

Dual-frequency imaging using an electrically tunable terahertz quantum cascade laser

Paul Dean,* Nor Kamila Saat, Suraj P. Khanna, Mohammed Salih, Andrew Burnett, John Cunningham, Edmund H. Linfield, and A. Giles Davies

School of Electronic and Electrical Engineering, University of Leeds, Leeds, LS2 9JT, UK

**p.dean@leeds.ac.uk*

Abstract: We report dual-frequency transmission imaging of polycrystalline materials using an electrically tunable terahertz (THz) frequency quantum cascade laser (QCL). Using our system we are able to obtain images at both 3.05 THz and 3.24 THz in a single two-dimensional scan of a sample. By taking the difference of the natural logarithms of the transmission coefficients obtained at each frequency, the difference-attenuation coefficient is determined, and evaluated for samples of lactose monohydrate, glucose monohydrate, sucrose, and the high explosive PETN. We also demonstrate difference-intensity imaging at these frequencies by combining amplitude modulation of the QCL bias with lock-in detection. Owing to the specific molecular absorption spectra of these materials in the THz frequency range, the samples can be distinguished using our technique.

©2009 Optical Society of America

OCIS codes: (110.6795) Terahertz imaging; (140.5965) Semiconductor lasers, quantum cascade (280.1350)

References and links

1. B. B. Hu, and M. C. Nuss, "Imaging with terahertz waves," *Opt. Lett.* **20**(16), 1716–1718 (1995).
2. V. P. Wallace, A. J. Fitzgerald, S. Shankar, N. Flanagan, R. J. Pye, J. Cluff, and D. D. Arnone, "Terahertz pulsed imaging of basal cell carcinoma ex vivo and in vivo," *Br. J. Dermatol.* **151**(2), 424–432 (2004).
3. S. M. Kim, F. Hatami, J. S. Harris, A. W. Kurian, J. Ford, D. King, G. Scaliari, M. Giovannini, N. Hoyler, J. Faist, and G. Harris, "Biomedical terahertz imaging with a quantum cascade laser," *Appl. Phys. Lett.* **88**(15), 153903–153905 (2006).
4. D. J. Cook, B. K. Decker, G. Dadusc, and M. G. Allen, "Through container THz sensing: applications for bio detection," *Proc. SPIE Int. Soc. Opt. Eng.* **5268**, 36–42 (2004).
5. K. Kawase, Y. Ogawa, Y. Watanabe, and H. Inoue, "Non-destructive terahertz imaging of illicit drugs using spectral fingerprints," *Opt. Express* **11**(20), 2549–2554 (2003), <http://www.opticsinfobase.org/abstract.cfm?URI=oe-11-20-2549>.
6. M. Lu, J. Shen, N. Li, Y. Zhang, C. Zhang, L. Liang, and X. Xu, "Detection and identification of illicit drugs using terahertz imaging," *J. Appl. Phys.* **100**(10), 103104–103106 (2006).
7. Y. C. Shen, T. Lo, P. F. Taday, B. E. Cole, R. Tribe, and M. C. Kemp, "Detection and identification of explosives using terahertz pulsed spectroscopic imaging," *Appl. Phys. Lett.* **86**(24), 241116–241118 (2005).
8. N. Karpowicz, H. Zhong, C. Zhang, K. Lin, J. Hwang, J. Xu, and X.-C. Zhang, "Compact continuous-wave subterahertz system for inspection applications," *Appl. Phys. Lett.* **86**(5), 054105–054107 (2005).
9. N. Karpowicz, H. Zhong, J. Xu, K. Lin, J. S. Hwang, and X.-C. Zhang, "Comparison between pulsed terahertz time-domain imaging and continuous wave terahertz imaging," *Semicond. Sci. Technol.* **20**(7), S293–S299 (2005).
10. H. Zhong, A. Redo-Sanchez, and X.-C. Zhang, "Identification and classification of chemicals using terahertz reflective spectroscopic focal-plane imaging system," *Opt. Express* **14**(20), 9130–9141 (2006), <http://www.opticsinfobase.org/oe/abstract.cfm?URI=oe-14-20-9130>.
11. Y. Watanabe, K. Kawase, T. Ikari, H. Ito, Y. Ishikawa, and H. Minamide, "Component spatial pattern analysis of chemicals using terahertz spectroscopic imaging," *Appl. Phys. Lett.* **83**(4), 800–802 (2003).
12. A. Dobroui, M. Yamashita, Y. N. Ohshima, Y. Morita, C. Otani, and K. Kawase, "Terahertz imaging system based on a backward-wave oscillator," *Appl. Opt.* **43**(30), 5637–5646 (2004).
13. S. Mair, B. Gompf, and M. Dressel, "Microspectroscopy and imaging in the THz range using coherent CW radiation," *Phys. Med. Biol.* **47**(21), 3719–3725 (2002).
14. T. Kleine-Ostmann, P. Knobloch, M. Koch, S. Hoffmann, M. Breede, M. Hofmann, G. Hein, K. Pierz, M. Sperling, and K. Donhuijsen, "Continuous-wave THz imaging," *Electron. Lett.* **37**(24), 1461–1462 (2001).
15. R. Köhler, A. Tredicucci, F. Beltram, H. E. Beere, E. H. Linfield, A. G. Davies, D. A. Ritchie, R. C. Iotti, and F. Rossi, "Terahertz semiconductor-heterostructure laser," *Nature* **417**(6885), 156–159 (2002).

16. C. Walther, M. Fischer, G. Scalari, R. Terazzi, N. Hoyler, and J. Faist, "Quantum cascade lasers operating from 1.2 to 1.6 THz," *Appl. Phys. Lett.* **91**(13), 131122 (2007).
17. A. W. M. Lee, Q. Qin, S. Kumar, B. S. Williams, Q. Hu, and J. L. Reno, "Real-time terahertz imaging over a standoff distance (>25 meters)," *Appl. Phys. Lett.* **89**(14), 141125–141127 (2006).
18. S. Kumar, Q. Hu, and J. L. Reno, "186 K operation of terahertz quantum-cascade lasers based on a diagonal design," *Appl. Phys. Lett.* **94**(13), 131105–131107 (2009).
19. B. Williams, S. Kumar, Q. Hu, and J. L. Reno, "High-power terahertz quantum-cascade lasers," *Electron. Lett.* **42**(2), 89–90 (2006).
20. P. Dean, M. U. Shaukat, S. P. Khanna, S. Chakraborty, M. Lachab, A. Burnett, G. Davies, and E. H. Linfield, "Absorption-sensitive diffuse reflection imaging of concealed powders using a terahertz quantum cascade laser," *Opt. Express* **16**(9), 5997–6007 (2008), <http://www.opticsinfobase.org/oe/abstract.cfm?uri=OE-16-9-5997>.
21. A. W. M. Lee, B. S. Wil, S. Kumar, Qing Hu, and J. L. Reno, "Real-time imaging using a 4.3-THz quantum cascade laser and a 320 x 240 microbolometer focal-plane array," *IEEE Photon. Technol. Lett.* **18**(13), 1415–1417 (2006).
22. H. Luo, S. R. Laframboise, Z. R. Wasilewski, G. C. Aers, H. C. Liu, and J. C. Cao, "Terahertz quantum-cascade lasers based on a three-well active module," *Appl. Phys. Lett.* **90**(4), 041112 (2007).
23. M. A. Belkin, J. A. Fan, S. Hormoz, F. Capasso, S. P. Khanna, M. Lachab, A. G. Davies, and E. H. Linfield, "Terahertz quantum cascade lasers with copper metal-metal waveguides operating up to 178 K," *Opt. Express* **16**(5), 3242–3248 (2008), <http://www.opticsinfobase.org/abstract.cfm?URI=oe-16-5-3242>.
24. S. P. Khanna, M. Salih, P. Dean, A. G. Davies, and E. H. Linfield, "Electrically tunable terahertz quantum cascade laser with a heterogeneous active region," *Appl. Phys. Lett.* in press.
25. A. Burnett, W. Fan, P. Upadhy, J. Cunningham, E. H. Linfield, A. G. Davies, H. Edwards, T. Munshi, and A. O'Neil, "Analysis of drugs of abuse and explosives using terahertz time-domain and Raman spectroscopy," *Proc. SPIE Int. Soc. Opt. Eng.* **6549**, 61200 (2007).
26. J. Chen, Y. Chen, H. Zhao, G. J. Bastiaans, and X.-C. Zhang, "Absorption coefficients of selected explosives and related compounds in the range of 0.1-2.8 THz," *Opt. Express* **15**(19), 12060–12067 (2007), <http://www.opticsinfobase.org/abstract.cfm?URI=oe-15-19-12060>.
27. Y. C. Shen, P. F. Taday, and M. Pepper, "Elimination of scattering effects in soectral measurement of granulated materials using terahertz pulsed spectroscopy," *Appl. Phys. Lett.* **92**(5), 051103–051105 (2008).
28. M. Franz, B. M. Fischer, and M. Walther, "The Christiansen effect in terahertz time-domain spectra of coarse-grained powders," *Appl. Phys. Lett.* **92**(2), 021107 (2008).
29. C. V. Raman, "The theory of the Christiansen experiment," *Proc. Indian. Acad. Sci, Sect. A* **29**, 381–389 (1949).
30. J. R. Fletcher, G. P. Swift, D. C. Dai, J. A. Levitt, and J. M. Chamberlain, "Propagation of terahertz radiation through random structures: An alternative theoretical approach and experimental validation," *J. Appl. Phys.* **101**(1), 013102 (2007).

1. Introduction

Since the first demonstration of imaging at terahertz (THz) frequencies [1], there has been considerable interest in the development of THz imaging systems suitable for a diverse range of applications including biomedicine [2,3], biological and chemical sensing [4–7], and industrial inspection [8,9]. Unlike millimetre-wave imaging, THz radiation produces vibrational excitations in many organic and inorganic materials, thereby providing a contrast mechanism for their detection. THz imaging also offers improved spatial resolution compared to millimetre-wave techniques, owing to the shorter wavelengths used. Furthermore, many potential applications exploit the transparency of common non-polar materials, such as paper and plastic packaging, to THz radiation.

THz imaging with a spectroscopic capability has been previously demonstrated in both the time-domain [6,7,10] and the frequency-domain [11–14]. Time-domain techniques typically employ a near-infrared ultra-fast laser source for both THz generation and coherent detection. The frequency spectrum at each imaging pixel can then be obtained by Fourier analysis of the time-domain THz pulse. Such schemes have been demonstrated in both transmission [6] and reflection geometries [7,10], employing both full-field acquisition [10] and raster-scanning of the sample [6,7] for image construction. Whilst time-domain approaches can provide spectral information over a broad bandwidth (several THz), they typically suffer from low THz powers, slow acquisition rates and the reliance on expensive and bulky laser sources. Conversely, a range of narrowband tunable sources including THz-wave parametric oscillators [11], backward-wave oscillators [12,13] and two-colour external-cavity laser diodes [14] have been applied to frequency-domain spectroscopic imaging at THz frequencies. Whilst narrowband tunable sources are generally restricted to incoherent detection schemes, such systems have the advantage of superior frequency resolution, thereby providing much larger power densities at the target frequency. Further benefits include

compactness, less intensive post-acquisition processing and potentially faster acquisition rates. However, such sources also typically suffer from low powers or are restricted to sub-THz operating frequencies.

In recent years, the quantum cascade laser (QCL) [15] has attracted intense interest as a narrowband THz source. THz QCLs have been demonstrated with emission frequencies ranging from 1.2 to 5.0 THz [16,17], and with operating temperatures as high as 186 K being reported in pulsed mode [18]. Under cw operation, output powers exceeding 100 mW have been achieved [19]. The high powers of such sources, coupled with the possibility of tailoring the emission to frequencies that exhibit low atmospheric attenuation has enabled real-time imaging over stand-off distances exceeding 25 m [17]. In this case, the object under evaluation was suitably thin and exhibited low attenuation at THz frequencies. For imaging of bulky or highly absorbing samples, standoff imaging in a diffuse reflection geometry has been employed [20]. Real-time imaging in both a transmission and reflection geometry has also been demonstrated at near-video-rates (20 frames per second) through use of a microbolometer focal-plane array [21].

In this paper, we report dual-frequency spectroscopic imaging using an electrically tunable THz QCL for the first time. Transmission images of pressed pellets of lactose monohydrate, glucose monohydrate, sucrose and the high explosive pentaerythritol tetranitrate (PETN) are simultaneously acquired at frequencies of 3.05 THz and 3.24 THz using a single two-dimensional scan of each sample. By comparing these images, we demonstrate that pure samples can be readily distinguished from each other by virtue of their specific molecular absorption spectra. Measurements of the attenuation of samples at the two imaging frequencies, as well as measurements of the difference-attenuation, are also presented for pellets comprising samples diluted with polytetrafluoroethylene (PTFE) powder to a range of concentrations. These results are interpreted in terms of contributions to the attenuation from both material absorption and scattering, demonstrating that absorption is the dominant mechanism for attenuation. Finally, we report direct difference-intensity imaging of polycrystalline pellets at 3.05 THz and 3.24 THz using amplitude modulation of the QCL bias with lock-in detection. Using this scheme we demonstrate the distinction between samples of PETN and lactose monohydrate. The ability to control the lasing frequency electrically offers considerable advantages over the use of multiple sources. Primarily, the difficulties associated with multiple source alignment are eliminated, enabling a difference-intensity image to be acquired in a single scan of the sample. The work we describe is an important step towards the realisation of multiple-frequency spectroscopic imaging using a THz QCL.

2. Experimental technique

2.1 Terahertz quantum cascade laser

The THz QCL used for this work is based on a GaAs-AlGaAs three-well phonon-depopulation active module [22,23] that was processed into a semi-insulating surface-plasmon (SP) ridge waveguide. In our structure, which has been described in detail elsewhere [24], the gallium growth rate was systematically reduced by ~10% during (molecular beam) epitaxial growth of the active region. This resulted in a “heterogeneous cascade” active region consisting of 23 sections of 10 repeated periods; the first section of 10 periods was grown with a gallium growth rate of 1.064 $\mu\text{m/hr}$, the second set at 1.059 $\mu\text{m/hr}$, and each subsequent set was grown with a further 0.5% reduction in the growth rate until finally a rate of 0.94 $\mu\text{m/hr}$ was attained for the final twenty-third section. Consequently, the GaAs well thickness is reduced by ~10% through the active region. In addition, the mole fraction of aluminium in the barriers increases from 14.2% to 15.7% and the Si doping level from $4.7 \times 10^{16} \text{ cm}^{-3}$ to $5.3 \times 10^{16} \text{ cm}^{-3}$ over the active region. By varying the bias applied to this structure, the emission frequency can be varied from ~3.05 THz to ~3.40 THz. Whilst SP waveguide structures preclude the high-temperature operation possible with double-metal waveguides [23], the improved beam quality and smaller beam divergence associated with the SP waveguide lend themselves well to imaging applications.

The dimensions of the QCL ridge used for this study are 2.1 mm x 140 μm x 10 μm . The device was cooled to 15 K using a helium-cooled continuous-flow cryostat, and driven with 2 μs current pulses at a repetition rate of 10 kHz. Figure 1 shows the current-voltage and light-current characteristics measured in a dry atmosphere under these conditions. The inset to Fig. 1 shows emission spectra of the device obtained at peak driving biases of 14.2 V and 16.2 V, measured using a Bruker IFS-66 Fourier transform spectrometer. For these two biases, emission is achieved predominantly at frequencies of 3.05 THz and 3.24 THz, respectively. This device operates up to a temperature of 85 K in pulsed mode, making possible the exploitation of liquid nitrogen cooling.

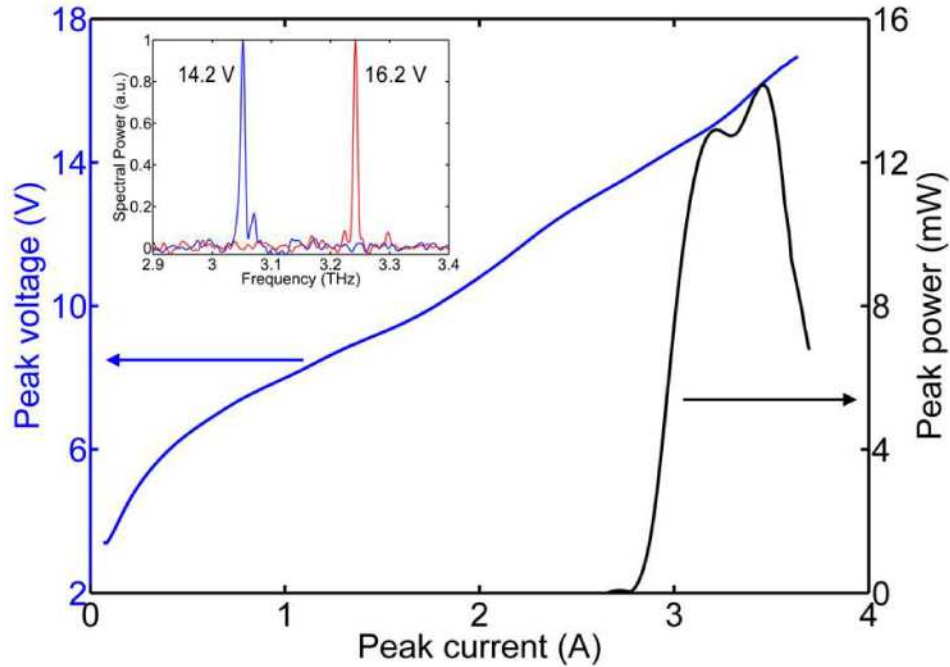


Fig. 1. Current-voltage (blue, left axis) and light-current (black, right axis) characteristics of the QCL used for this study, driven by 2 μs pulses at a repetition rate of 10 kHz and a temperature of 15 K. The dimensions of the QCL are 2.1 mm x 140 μm x 10 μm . Inset: Emission spectra obtained at peak driving biases of 14.2 V (blue) and 16.2 V (red).

2.2 Dual-frequency imaging

Figure 2 shows a schematic diagram of the imaging apparatus. Radiation from the QCL was collimated using a 3-inch-diameter $f/2$ off-axis parabolic reflector and focussed onto the sample using a second $f/2$ reflector. The radiation transmitted through the sample was collected and coupled into a helium-cooled silicon bolometer using additional $f/2$ reflectors. For image acquisition the sample was mounted on a computer-controlled two-axis translation stage and raster-scanned with a step-size of 250 μm . At each sample position the QCL driving bias was switched between 14.2 V and 16.2 V, and the detector response recorded for each bias. The train of driving pulses was modulated at a frequency of ~ 190 Hz, with lock-in detection used to improve the detection sensitivity. Samples were measured in ambient atmosphere rather than using dried purging gas, to widen the applicability of our measurements. Samples were prepared by mechanical grinding to a particle size < 50 μm , diluting with 55- μm -diameter PTFE powder, and then mechanical pressing into pellets of diameter 8 mm and thickness ~ 0.5 mm.

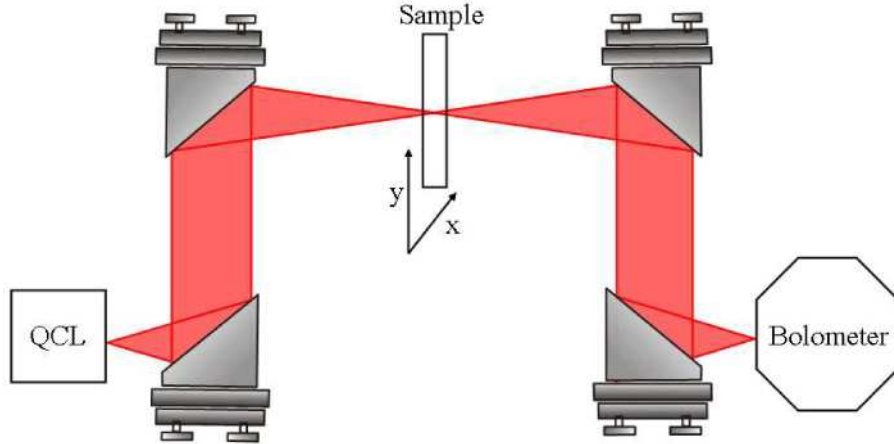


Fig. 2. Experimental apparatus used for dual-frequency imaging with a quantum cascade laser. The arrows indicate two-dimensional raster scanning.

By scanning a knife edge across the THz beam, the beam diameter at the position of the sample was found to be <1 mm at both 3.05 THz and 3.24 THz, with negligible astigmatic difference at either frequency. The peak powers incident on the sample were measured to be ~ 2.6 mW and ~ 5.0 mW at these frequencies, respectively. By measuring the detector response with the THz beam blocked, the detection dynamic ranges were found to be ~ 47 dB and ~ 49 dB for a lock-in time constant of 10 ms. We note that these values can be increased at the expense of the imaging rate by longer integration of the detector output. For example, dynamic ranges of ~ 62 dB and ~ 64 dB can be achieved with a time constant of 1 s.

3. Results and discussion

3.1 Dual-frequency imaging

Figures 3(a) and 3(b) show transmission images of a pellet comprising 26% by volume (26-vol %) of the high explosive PETN diluted with PTFE, acquired at 3.05 THz and 3.24 THz, respectively. Both images are normalised to the incident beam power. The image size is 44×44 pixels, corresponding to an area measuring 11 mm \times 11 mm. As can be seen, greater transmittance is observed at 3.24 THz compared to 3.05 THz. The mean sample transmittance at each frequency was measured by sampling over a 5 mm \times 5 mm (20×20 pixels) region in the centre of the pellet to reduce the effects of laser speckle and inhomogeneity within the sample. These measured values include transmission losses arising from reflections at the air-pellet interfaces as well as attenuation caused by absorption and scattering within the pellet. Expressing the total attenuation per unit thickness as β , the transmittance can be related to the sample thickness L according to the relation

$$T = (1 - R)^2 \exp(-\beta L), \quad (1)$$

where R is the Fresnel reflection coefficient. For our samples, R is estimated to be ≤ 0.05 and can therefore be neglected. For the PETN pellet shown in Fig. 3, attenuation coefficients $\beta_{3.05} = 29.9 \pm 3.3 \text{ cm}^{-1}$ and $\beta_{3.24} = 16.9 \pm 1.9 \text{ cm}^{-1}$ are calculated at 3.05 THz and 3.24 THz, respectively. The uncertainty in these values has been estimated from the variance of the 400 sampled pixel values. The greater attenuation measured at 3.05 THz compared to 3.24 THz is consistent with the attenuation spectrum of the PETN sample, obtained using THz time-domain spectroscopy (TDS) [25] and shown in Fig. 4. This spectrum exhibits a strong resonant absorption peaked at ~ 2.85 THz [26], which gives rise to a decreasing attenuation with increasing frequency in the range 2.9 THz to 3.7 THz. We note, however, that the attenuation coefficients obtained from this time-domain spectrum are larger than those measured using the QCL imaging system. We attribute this discrepancy to the fact that, owing

to the long acquisition times required, the time-domain spectra were obtained at only one position on the pellet. As such, the PETN spectrum is susceptible to sample inhomogeneities arising from improper mixing within this two-component pellet.

The lower attenuation at the higher imaging frequency for the PETN pellet is also evident from the difference-transmission image (Fig. 3(c)), defined as the difference between the transmission images obtained at the two imaging frequencies, $T_{3.24} - T_{3.05}$. For the PETN sample this difference has a positive value. Conversely, for a sample of pure lactose monohydrate, this difference has a negative value, as shown in Fig. 3(d), as this sample exhibits greater attenuation at 3.24 THz than at 3.05 THz (Fig. 4). The differences between the spectra of PETN and lactose monohydrate thus enable these samples to be distinguished from each other by their difference-transmission images.

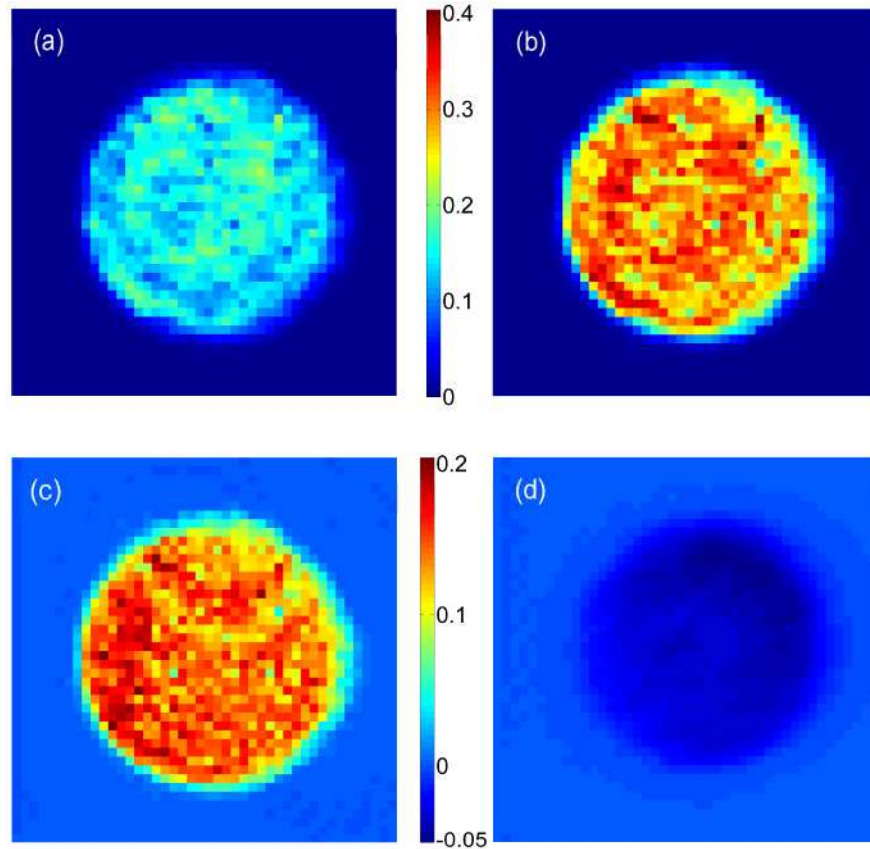


Fig. 3. Transmission images of a pellet containing 26-vol % PETN taken at (a) 3.05 THz and (b) 3.24 THz. Both images are normalised to the incident power. Difference transmission $T_{3.24} - T_{3.05}$ image of (c) the PETN pellet and (d) a pure lactose monohydrate pellet. Images (a) and (b), and (c) and (d), are shown on the same colour scales.

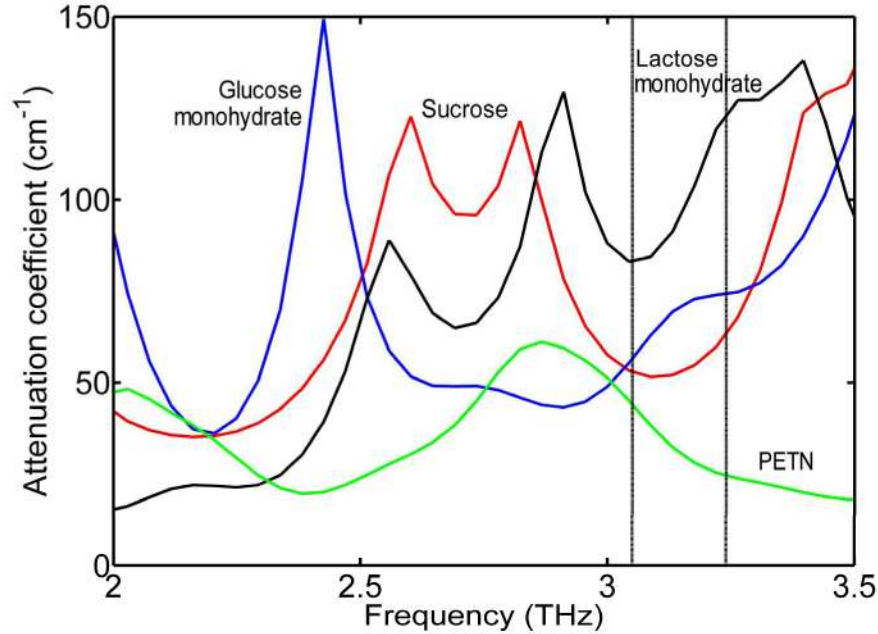


Fig. 4. Attenuation spectra of pellets containing (a) 26-vol % PETN (green), lactose monohydrate (black), glucose monohydrate (blue) and sucrose (red), obtained using terahertz time-domain spectroscopy in a purged environment. The spectral resolution is ~ 150 GHz; 4-times zero-padding has been applied. The QCL imaging frequencies are indicated by the vertical black lines.

3.2 Difference-attenuation imaging

The ability to obtain dual-frequency images enables samples of different chemical composition to be distinguished. By taking the difference of the natural logarithms of the transmission coefficients obtained for each pixel [$\ln(T_{3.24}) - \ln(T_{3.05})$], an image representing the difference-attenuation $(\beta_{3.05} - \beta_{3.24})L$ for each sample is obtained via Eq. (1). This is shown in Fig. 5(a) for the case of the PETN pellet. The positive value seen here again implies greater sample attenuation at 3.05 THz. From this image, the difference-attenuation coefficient $\Delta\beta = (\beta_{3.05} - \beta_{3.24})$ for the sample can be readily obtained using the measured pellet thickness. In this case a value of $\Delta\beta = 13.1 \pm 1.9 \text{ cm}^{-1}$ is found.

Figures 5(b)–5(d) show the difference-attenuation images for samples of pure lactose monohydrate, glucose monohydrate, and sucrose, respectively. In contrast to the difference-attenuation image obtained for the PETN pellet, all of these images have negative values, indicating greater sample attenuation at 3.24 THz than at 3.05 THz. These results are consistent with the TDS spectra obtained for these samples, all of which exhibit increasing attenuation between 3.0 THz and 3.3 THz as shown in Fig. 4. We note that the samples of sucrose and glucose monohydrate are not readily distinguishable in Fig. 5, but this is a consequence of the colour scale adopted. It should also be noted that all images shown in Fig. 3 and Fig. 5 were acquired and displayed in real-time by our system during a single two-dimensional raster scan of the sample.

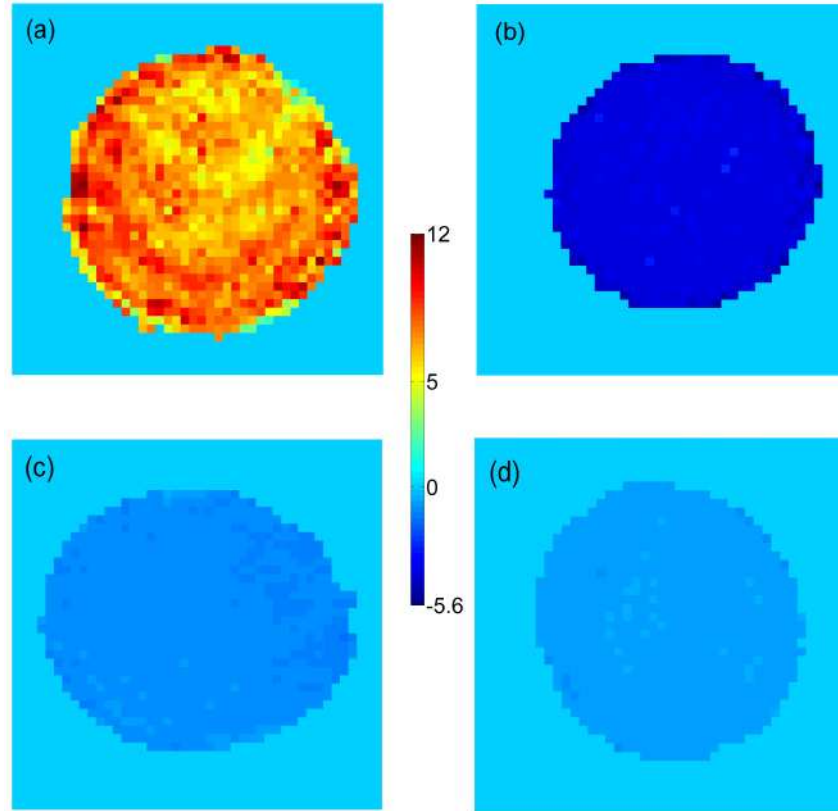


Fig. 5. Difference-attenuation $[\ln(T_{3.24}) - \ln(T_{3.05})]$ image of pellets of (a) 26-vol % PETN, (b) pure lactose monohydrate, (c) pure glucose monohydrate and (d) pure sucrose. Image (a) has been multiplied by a factor of ten for clarity.

Figure 6 summarises the values of $\Delta\beta$ measured for samples of lactose monohydrate, PETN, glucose monohydrate, and sucrose, diluted to a range of concentrations with PTFE powder. The volume fraction of absorbing compound has been estimated for each pellet using the measured mass fractions in the pellet mixture and the known relative densities of the constituents. The volume fraction of PETN used is restricted to $< 26\%$ to prevent explosion during sample preparation. Once again, the error bars have been estimated from the variance of the sampled image pixels. Negative values of $\Delta\beta$ are obtained for the lactose monohydrate, glucose monohydrate and sucrose samples, whereas in the case of PETN, a positive value is observed. The sign of $\Delta\beta$ arises predominantly from the molecular-specific absorption spectra of the materials studied.

The measured sample attenuation is expected to contain contributions arising from absorption within the sample together with losses owing to radiation that is scattered out of the field-of-view of the collection optics. For pellets containing a weakly absorbing matrix, such as PTFE, the absorption contribution will vary approximately linearly with the volume fraction of absorbing material. Scattering events may occur at interfaces between powder and the surrounding medium (air) [27], as well as at interfaces between the absorbing powder and the matrix powder (PTFE). The latter of these scattering mechanisms leads to a phenomenon known as the *Christiansen effect* [28,29]. It can be shown that this results in a sample attenuation proportional to the factor $c(1-c)$ for a two-material mixture, where c is the volume fraction of either material [29,30]. Air-powder scattering within the bulk of the pellet is anticipated to be small in our samples owing to the small particle size and compressed form of the pellets [27]. Indeed, measurements on a pellet made from 100% PTFE powder yield attenuation coefficients $\beta_{3.05} \cong \beta_{3.24} \cong 4 \text{ cm}^{-1}$; a value close to the expected absorption

coefficient for this material, which confirms minimal internal air-powder scattering. Therefore, the total attenuation coefficient for our samples, relative to that of a PTFE pellet, can be approximated by the relationship

$$\beta = \alpha_0 c + 4\mu_0 c(1 - c). \quad (2)$$

in which α_0 is the absorption coefficient for a pure pressed pellet of the absorbing material. The factor μ_0 is the upper limit for the effective scattering coefficient (i.e. realised in a mixture with $c = 0.5$), which will depend on the shape and size of the scattering centres, as well as the refractive index mismatch between the absorbing particles and the host medium [29]. Accordingly, the difference-attenuation coefficient $\Delta\beta$ for a given sample, obtained from the difference of the natural logarithms of the transmission coefficients obtained at the two imaging frequencies, can be expressed in the same form as Eq. (2) with the attenuation and scattering coefficients α_0 and μ_0 replaced by the difference coefficients $\Delta\alpha_0 = (\alpha_0^{3.05} - \alpha_0^{3.24})$ and $\Delta\mu_0 = (\mu_0^{3.05} - \mu_0^{3.24})$.

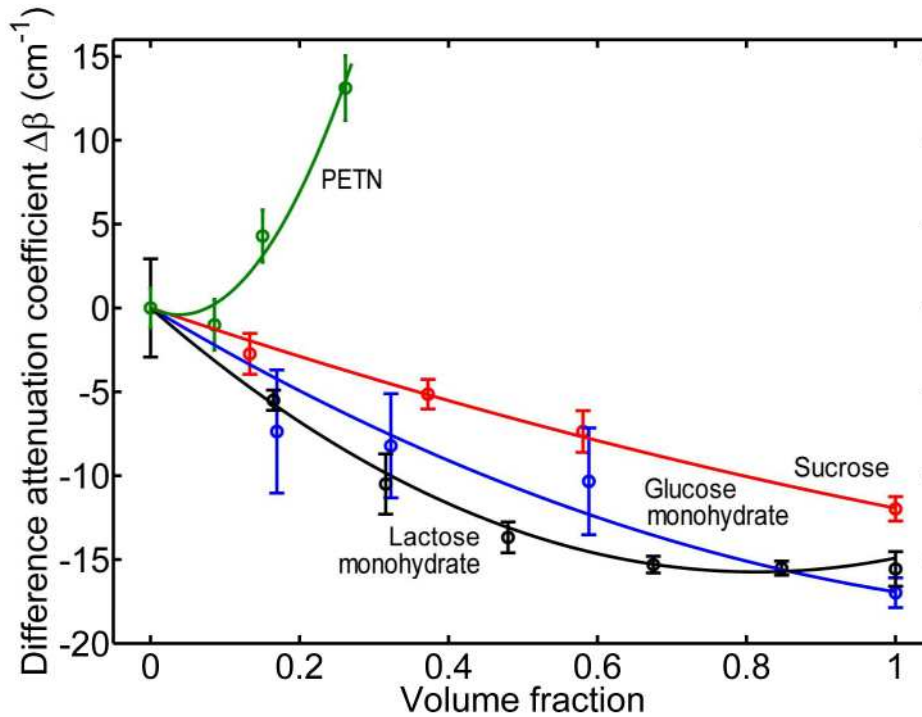


Fig. 6. Difference-attenuation coefficients $\Delta\beta = (\beta_{3.05} - \beta_{3.24})$ measured for samples of PETN (green), lactose monohydrate (black), glucose monohydrate (blue) and sucrose (red), diluted with PTFE. The solid lines are least-squares fits to Eq. (2). The data for lactose monohydrate has been divided by 5 for clarity.

The solid lines shown in Fig. 6 represent least-squares fits of this expression to the data, with $\Delta\alpha_0$ and $\Delta\mu_0$ treated as free parameters. For the cases of lactose monohydrate, sucrose and glucose monohydrate, difference-attenuation coefficients $\Delta\alpha_0 = -75 \pm 10 \text{ cm}^{-1}$, $-12 \pm 3 \text{ cm}^{-1}$ and $-17 \pm 4 \text{ cm}^{-1}$ are obtained, respectively. These negative values indicate greater absorption at 3.24 THz than at 3.05 THz, as confirmed by TDS measurements (see Fig. 4). Conversely, a positive value $257 \pm 90 \text{ cm}^{-1}$ is obtained for PETN, as expected from the absorption spectrum for this material. For sucrose and glucose monohydrate, difference-scattering coefficients $\Delta\mu_0 \cong 0$ are obtained, which confirms a minimal contribution to the difference-attenuation from scattering in these cases. This is also evident from the near-linear form of the data shown for these materials. For lactose monohydrate and PETN, the values

$\Delta\mu_0 = -30 \pm 2 \text{ cm}^{-1}$ and $-70 \pm 22 \text{ cm}^{-1}$ are found. These negative values indicate stronger scattering at the higher frequency, as expected for a small particle size compared to the radiation wavelength. We note that the consistently smaller magnitudes of $\Delta\mu_0$ relative to $\Delta\alpha_0$ confirms that frequency-dependent absorption is the dominant mechanism contributing to the difference-attenuation coefficients measured for all samples studied.

3.3 Difference-intensity imaging by amplitude modulation and lock-in detection

Using our imaging apparatus, difference-intensity images can be acquired by amplitude modulation of the QCL bias and lock-in detection at this modulation frequency. The QCL is driven by a train of 2- μs -long pulses at a repetition rate of 10 kHz, which is gated by a square wave at $\sim 190 \text{ Hz}$. The amplitude of the 2 μs pulses is also modulated between the two biases (14.2 V and 16.2 V) at a rate $\sim 10 \text{ Hz}$. In our system, this amplitude modulation is controlled by computer software, with a digital acquisition card employed to generate a TTL pulse for use as a reference waveform in the lock-in amplifier. With this scheme, raster-scanning of the sample does not need to be synchronised with the QCL driving electronics. However, it is not possible to obtain two separate single-frequency images; the magnitude of the lock-in output R corresponds to the magnitude of the difference-intensity $|I_{3.24} - I_{3.05}|$ with the phase θ providing its sign. We also note that, owing to the processing time of the computer, stable locking of the detector output to this signal was only possible for modulation frequencies $\leq 18 \text{ Hz}$ in our setup.

Figure 7 shows difference-intensity images of the same lactose monohydrate and PETN samples used for Fig. 3. Here, the colour scale corresponds to the real part of the lock-in output $R\cos(\theta)$. For the lactose monohydrate sample, the mean phase $\theta \sim \pi$ results in negative pixel values, enabling this to be distinguished from the PETN sample for which $\theta \sim 0$. For these measurements, a 200-ms time constant was used in the lock-in amplifier and the measurement time was 1 second for each pixel.

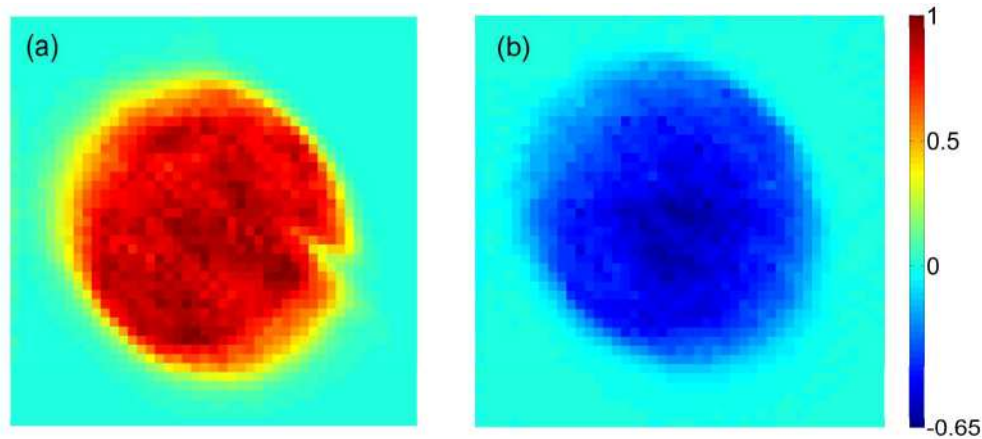


Fig. 7. Difference-intensity $I_{3.24} - I_{3.05}$ transmission images of pellets containing (a) 26-vol % PETN and (b) pure lactose monohydrate, obtained at an amplitude modulation frequency of 10 Hz. Both images have been normalised to the difference-intensity measured for the PETN pellet. Image (b) has been multiplied by a factor of ten for clarity.

4. Conclusions

In summary, we have demonstrated dual-frequency imaging of polycrystalline samples using an electrically tunable THz QCL and obtained images at 3.05 THz and 3.24 THz in a single raster scan of a sample. By taking the difference of the natural logarithms of the transmission coefficients obtained at each frequency, difference-attenuation coefficient images for samples of lactose monohydrate, glucose monohydrate, sucrose and the high explosive PETN were obtained. Furthermore, we have successfully demonstrated difference-intensity imaging by

combining amplitude modulation of the QCL bias with lock-in detection. Owing to their unique molecular-specific absorption spectra, the samples measured could be readily distinguished using our system. This work demonstrates the applicability of THz QCL sources to spectroscopic imaging, and is an important step towards the demonstration of multiple-frequency spectroscopic imaging using such a source.

Acknowledgements

We acknowledge support from the EPSRC (UK), EC (NOTES programme), the Government of Malaysia, Her Majesty's Government Communications Centre, the Defence Science and Technology Laboratory, HM Revenue and Customs, the Home Office Scientific Development Branch, and the Forensic Science Service.